

Molybdenum Disulfide Nanowires and Nanoribbons by Electrochemical/Chemical Synthesis

Q. Li,[†] E. C. Walter,[†] W. E. van der Veer,[†] B. J. Murray,[†] J. T. Newberg,[†] E. W. Bohannon,[‡] J. A. Switzer,[‡] J. C. Hemminger,[†] and R. M. Penner^{*,†}

Department of Chemistry, University of California, Irvine, California 92679-2025, and
Department of Chemistry and Graduate Center for Materials Research, University of Missouri—Rolla,
Rolla, Missouri 65409-1170

Received: October 31, 2004; In Final Form: November 21, 2004

Molybdenum disulfide nanowires and nanoribbons have been synthesized by a two-step, electrochemical/chemical synthetic method. In the first step, MoO_x wires (a mixture of MoO₂ and MoO₃) were electrodeposited size-selectively by electrochemical step-edge decoration on a highly oriented pyrolytic graphite (HOPG) surface. Then, MoO_x precursor wires were converted to MoS₂ by exposure to H₂S either at 500–700 °C, producing “low-temperature” or LT MoS₂ nanowires that were predominantly 2H phase, or above 800 °C producing “high-temperature” or HT MoS₂ ribbons that were predominantly 3R phase. The majority of these MoS₂ wires and ribbons were more than 50 μm in length and were organized into parallel arrays containing hundreds of wires or ribbons. MoS₂ nanostructures were characterized by X-ray photoelectron spectroscopy, scanning and transmission electron microscopy, selected area electron diffraction, X-ray diffraction, UV–visible absorption spectrometry, and Raman spectroscopy. HT and LT MoS₂ nanowires were structurally distinct: LT MoS₂ wires were hemicylindrical in shape and nearly identical in diameter to the MoO_x precursor wires from which they were derived. LT MoS₂ wires were polycrystalline, and the internal structure consisted of many interwoven, multilayer strands of MoS₂; HT MoS₂ ribbons were 50–800 nm in width and 3–100 nm thick, composed of planar crystallites of 3R-MoS₂. These layers grew in van der Waals contact with the HOPG surface so that the *c*-axis of the 3R-MoS₂ unit cell was oriented perpendicular to the plane of the graphite surface. Arrays of MoS₂ wires and ribbons could be cleanly separated from the HOPG surface and transferred to glass for electrical and optical characterization. Optical absorption measurements of HT MoS₂ nanoribbons reveal a direct gap near 1.95 eV and two exciton peaks, A1 and B1, characteristic of 3R-MoS₂. These exciton peaks shifted to higher energy by up to 80 meV as the wire thickness was decreased to 7 nm (eleven MoS₂ layers). The energy shifts were proportional to 1/*L*_t², and the effective masses were calculated. Current versus voltage curves for both LT and HT MoS₂ nanostructures were probed as a function of temperature from –33 °C to 47 °C. Conduction was ohmic and mainly governed by the grain boundaries residing along the wires. The thermal activation barrier was found to be related to the degree of order of the crystallites and can be tuned from 126 meV for LT nanowires to 26 meV for HT nanoribbons.

I. Introduction

Semiconductor nanowires have been used as the basis for a variety of devices including diodes,^{1–11} light-emitting diodes,^{8,11–14} photodetectors,^{11,15,16} transistors,^{6,17–19} digital logic gates,¹⁹ lasers,^{20–26} and chemical sensors.^{27,28} A practical issue that has not yet received much attention is the vulnerability of nanowires to oxidation, particularly in chemical sensing which can require the exposure of a nanowire for extended periods to aqueous solutions or humid air. This vulnerability is a consequence of the instability of all group IV (e.g., silicon), III–V (e.g., GaAs), or II–VI (e.g., CdS) semiconductors in either water or humid air at room temperature.^{cf.29–33} MoS₂ is similar in its electronic properties to silicon (an indirect band gap of 1.2 eV versus 1.12 eV for silicon), but it is composed of S–Mo–S layers, disposed in van der Waals contact, with coordinately saturated surfaces that resist oxidation even at temperatures up to 85 °C³⁴ and under illumination in water.^{35–38} Superior environmental stabil-

ity constitutes a clear advantage for the application of MoS₂ nanoparticles and nanowires.

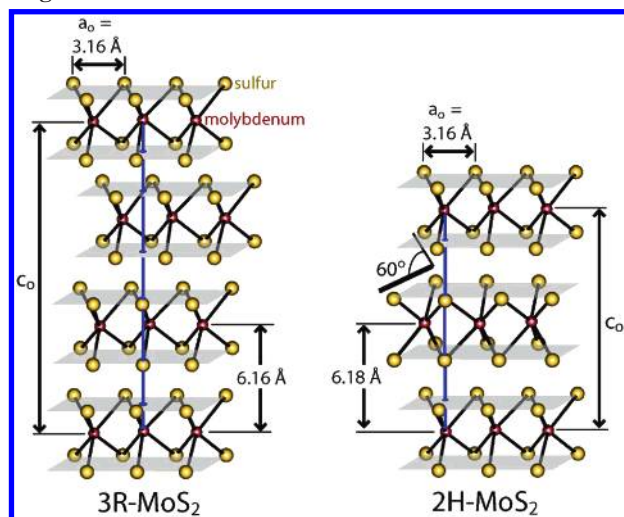
Tenne and co-workers were the first to describe the synthesis of fullerene MoS₂ nanotubes in 1995.^{39,40} Their synthesis involved the reaction of MoO₃ micron-scale particles with H₂S at 800–950 °C.^{39,40} Soon thereafter, MoS₂ “microtubes” with diameters of several microns and single-walled MoS₂ fullerene nanotubes were both synthesized by iodine vapor transport of MoS₂ powder in a vacuum at 740 °C by Remskar et al.^{41–44} Later, Zelenski and Dorhout⁴⁵ synthesized MoS₂ nanotubes by the thermal decomposition of ammonium thiomolybdate molecular precursors at 450 °C. Nanotubes have also been prepared by the sublimation of 2H-MoS₂ powder in the presence of H₂S at 1300 °C by Hsu et al.⁴⁶

Non-fullerene nanoparticles of MoS₂ have also been prepared by several methods including the dissolution of MoS₂ in acetonitrile at 35–60 °C,⁴⁷ chemical synthesis inside inverse micelles,^{48–50} and as a byproduct of attempts to prepare fullerene nanoparticles by gas-phase vapor transport,^{e.g.,40,51,52} but little direct structural information has been reported for these non-fullerene MoS₂ nanoparticles.

* Address correspondence to rmpenner@uci.edu.

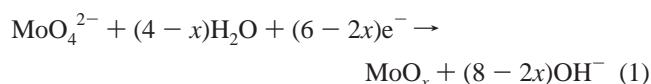
[†] University of California.

[‡] University of Missouri—Rolla.

SCHEME 1: Schematic Diagram Illustrating the Structures of 3R- and 2H-MoS₂. Distances on This Diagram Are Not to Scale

In a recent communication,⁵³ we reported a two-step electrochemical/chemical (E/C) synthesis^{54,55} of non-fullerene, polycrystalline MoS₂ nanowires and nanoribbons. In this full paper, the details of this synthesis and the structural, optical, and electrical properties of the resulting MoS₂ wires and ribbons are reported. MoS₂ exists in four distinct polytypes: Rhombohedral (3R-MoS₂) and hexagonal (2H-MoS₂) are found in the naturally occurring mineral molybdenite. Tetragonal (1T-MoS₂) is observed only for single layers exfoliated from 2H- or 3R-MoS₂ crystals⁵⁶ and fullerene MoS₂ (IF-MoS₂) already discussed above. Both 3R- and 2H-MoS₂ are composed of covalently bound S–Mo–S layers in which a molybdenum is located in trigonal prismatic coordination with six sulfurs, three above the Mo atom and three below it. These S–Mo–S layers are stacked in van der Waals contact with one another along the *c*-axis of the material. It is the details of this stacking that distinguish the 3R and 2H polytypes, as shown in Scheme 1. Specifically, adjacent layers in the 2H polytype are rotated by 60°, whereas adjacent layers in the 3R polytype can be superimposed with a translation only. 3R- and 2H-MoS₂ are both semiconductors with an indirect band gap of 1.2 eV and a direct band gap at 1.95 eV.⁵⁷

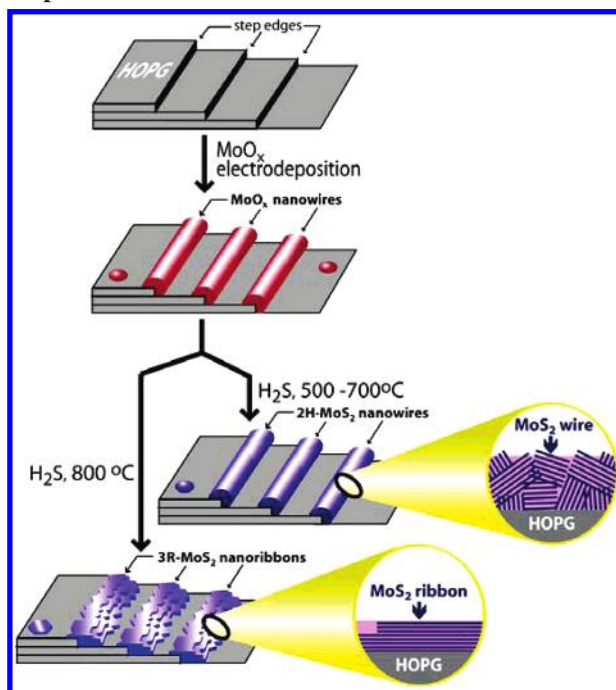
We prepared MoS₂ nanowires according to the procedure shown in Scheme 2. In the first step, amorphous MoO_x nanowires were electrodeposited by electrochemical step-edge decoration (ESED) onto highly oriented pyrolytic graphite surfaces according to the reaction^{58,59}



In the second step, these MoO_x nanowires were converted to MoS₂ by exposure to H₂S within either of two temperature regimes (500–700 °C or 800–1000 °C) according to the reaction (for *x* = 2 in eq 1)



As indicated in Scheme 2, conversion from MoO_x to MoS₂ within these two temperature regimes produced wires with different morphologies: Conversion of MoO_x wires at 500–700 °C yielded hemicylindrical wires that were nearly identical in diameter to the MoO_x precursor wires. These low-temperature

SCHEME 2: The E/C Method for Synthesizing Polycrystalline MoS₂ Nanowires and Nanoribbons on Graphite Surfaces

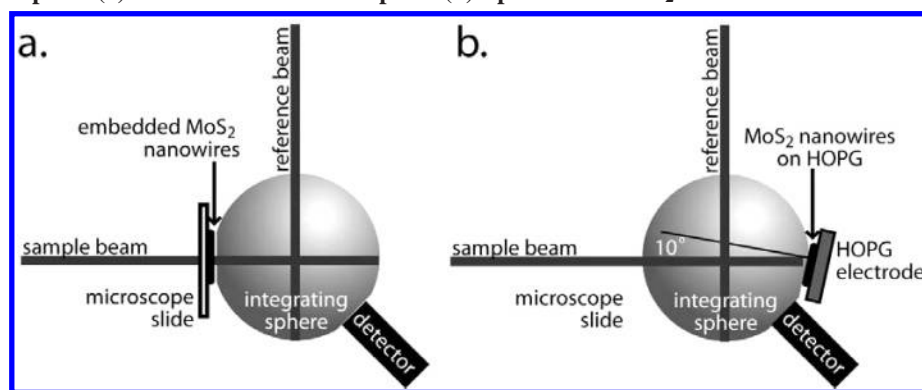
or LT MoS₂ wires were composed of multiple, interwoven 2H-MoS₂ strands with widths of 7–16 nm and lengths of up to hundreds of nanometers. At higher temperatures of 800–1000 °C, conversion to MoS₂ was followed by rapid grain growth that produced highly crystalline HT MoS₂ wires or “ribbons” that were hundreds of microns in length, 50–800 nm in width, and 3–100 nm in thickness. The absorption spectroscopy of these nanoribbons indicates they are composed of 3R-MoS₂. The E/C synthesis of MoS₂ wires and ribbons was size-selective: Control over the wire or ribbon size was provided by control of the MoO_x nanowire dimensions, which in turn were controlled using the electrodeposition potential and time in the first step of the synthesis. In this paper, we provide a detailed description of this new method, and we disclose our results relating to the structural, optical, and electrical properties of the MoS₂ wires we have prepared.

II. Experimental Section

II.A. Molybdenum Oxide Nanowire Electrodeposition.

Molybdenum oxide nanowires were electrodeposited from aqueous plating solutions containing Na₂MoO₄ (0.1–10 mM, 98+% anhydrous, Aldrich), 1.0 M NaCl (Fischer certified ACS grade), and 1.0 M NH₄Cl (J. T. Baker) adjusted to pH 8.5 using aqueous ammonium hydroxide (Fischer ACS grade) and purged with N₂ for 30 min prior to each experiment. These solutions were prepared using Barnsted Nanopure water (*ρ* > 17 MΩ cm^{−1}). A basal-plane-oriented, 12 × 12 × 1 mm³ piece of HOPG was employed as the working electrode in a three-electrode cell with a large-area platinum counter electrode and a saturated calomel reference electrode (SCE). The HOPG electrode was held in a Teflon holder in which a rubber O-ring isolated a 3.3 mm diameter area of the HOPG basal plane for exposure to the plating solution. Nanowire electrodeposition and cyclic voltammetry were both performed using a computer-controlled EG&G 2263 potentiostat.

II.B. Conversion of MoO_x to MoS₂ and Removal from HOPG. Nanowires prepared using the procedure described

SCHEME 3: Schematic Diagrams Showing the Implementation of an Integrating Sphere for the Acquisition of Transmission–Absorption (a) and Reflection–Absorption (b) Spectra for MoS₂ Nanowires

above were composed of molybdenum oxide (see discussion below). The conversion of MoO_x nanowires to MoS₂ nanowires was effected by heating the graphite working electrode in a tube furnace at 500–1000 °C under flowing H₂S for 5–84 h. The converted MoS₂ nanowires were lifted off the graphite surface using the following procedure: a drop of cyanoacrylate was put onto a microscope slide, and the HOPG with nanowires was pressed into contact with the cyanoacrylate drop. Then, the sample was left overnight to permit the droplet to harden. The HOPG was peeled off, and the majority of the nanowires were embedded in the cyanoacrylate film.

II.C. X-ray Photoelectron Spectroscopy. X-ray photoelectron spectroscopy (XPS) was carried out using an ESCALAB MKII photoelectron spectrometer (VG Scientific). The ESCALAB MKII is a multitechnique surface analysis instrument based on an ultrahigh vacuum (UHV) system consisting of three separately pumped, interconnected chambers (sample preparation, fast sample entry, and spectroscopy). The fast-entry chamber allowed rapid sample transfer from air to UHV pressures (base pressures during XPS analysis were in the low-to-mid 10^{−10} Torr range). The XPS experiments were performed in the spectroscopy chamber using a standard Mg anode X-ray source (Mg Kα line at 1253.6 eV) and a 150 mm hemispherical electron energy analyzer. The spectra presented here were obtained using an analyzer pass energy of 20 eV. Under these conditions, the spectrometer energy resolution was ~0.8 eV. The XPS energy scale is referenced to a binding energy of 284.5 eV for the C(1s) peak of graphite.⁶⁰

II.D. Powder X-ray Diffraction. Powder X-ray diffraction was carried out using either of two diffractometers: a Philips X'Pert Materials Research and a Siemens D5000. Both instruments were operated with a Cu source using line focus. For patterns acquired using the Philips X'Pert diffractometer, the incident beam optic module was an X-ray mirror (Philips, PW3088/60), while the secondary optic module was a 0.18° parallel-plate collimator (Philips, PW3098/18). For the fast scans, the incident angle was fixed at 1°, and data was acquired in the continuous mode every 0.03° with a counting time of 4 s per point over the range 5–70° 2θ. Slow scans were obtained with Ω fixed at 0.5° in the continuous mode with a step size of 0.03° and a count time of 30 s per point over the 2θ range from 25° to 56°. For the Siemens D5000, the optics consisted of a system of primary Soller foils and a system of secondary Soller foils. In the measurement, the sample rotates at a constant angular velocity, while the detector rotates at double angular velocity. For the fast scans, a step size of 0.05° and a count time of 1 s were used. For the slow scans, a step size of 0.02° and a count time of 5 s were used.

II.E. Electron Microscopy. Scanning electron microscopy (SEM) was carried out on uncoated or gold-coated samples using a Philips FEG-30XL microscope equipped with energy-dispersive analysis of x-rays (EDAX) elemental analysis capabilities. An accelerating voltage of 10 keV was used for SEM imaging, whereas for EDAX analysis, 20 keV was used. Transmission electron microscopy (TEM) was carried out using a Philips CM-20. HOPG flakes with attached nanowires were transferred to uncoated copper grids (uncoated copper, Ted Pella) for analysis using TEM. These flakes were obtained by mechanically scraping the HOPG surface with the grid.

II.F. Optical Absorption Spectroscopy. The optical absorption of the MoS₂ nanoribbons was measured using a Perkin-Elmer Lambda 900 UV–vis–NIR photospectrometer fitted with a tungsten halogen light source, a double monochromator, a photomultiplier, and a peltier-stabilized CdS detector. It was also equipped with a general purpose optical bench (GPOB) that contained an assembly for measuring surface reflectance with an integrating sphere (Lab Sphere, Inc.). The spectrometer uses a double beam configuration; the signal and the reference beams are both directed into the integrating sphere perpendicularly, through two apertures. For transmission measurement, the MoS₂ nanoribbons were first transferred to a transparent glass substrate and then placed in front of the aperture, as shown in Scheme 3a. The transparent glass coated with cyanoacrylate was used for a background scan before each transmission measurement. For reflection measurement, the HOPG with MoS₂ nanoribbons was mounted at an additional aperture at the rear of the sphere and was directly illuminated by the signal beam. The sample was mounted at a 10° angle, making the directly reflected (specular) beam strike the inside of the integrating sphere, which also captured the diffusely reflected radiation (Scheme 3b). A freshly cleaved HOPG was used as a background reference, and the resulting absorption signals were subtracted. In both transmission and reflection measurement, the spectrometer was scanned over the wavelength range 350–1200 nm, with bandwidth of 5 nm and a step size of 1 or 2 nm. The integration time per step was 5–10 s. At 700 nm, the grating in the spectrometer was changed from visible to NIR. At the same wavelength, the photodetector was changed between the photomultiplier and the CdS cell.

II.G. Raman Spectroscopy. Raman spectra are recorded using a microscope fitted with a spectrometer and a nitrogen-cooled charge-coupled device (CCD) detector. The sample is excited by a Coherent Innova 90-6 argon ion laser operating at 514.5 nm. The beam is focused to a diameter of 0.5 mm and directed, externally to the collection optics, onto the graphite surface at an angle of 65° from its normal. The sample is placed

in ambient air and maintained at room temperature. Light scattered from the surface of the sample is collected by a 20× Zeiss EpiPlan objective placed right above the sample. Rayleigh-scattered light is rejected using a holographic notch filter (Kaiser Notch-Plus); the remaining radiation, caused by inelastic scattering, is directed via an f4 lens into the spectrograph (Chromex 250IS, 1200 groove mm⁻¹ holographic grating, 500 nm blaze). The dispersed light is imaged onto a liquid nitrogen-cooled CCD (Princeton Instruments model LN/1024EUV) with 1024 × 256 pixels. The signals from the 256 pixels perpendicular to the dispersion direction were binned, effectively creating a linear detector with 1024 channels. In our present arrangement, the dispersion is 2.2 cm⁻¹ per pixel. The spectrograph was calibrated using the emission lines of a mercury lamp. This calibration was verified by confirming the positions of the ν_{N_2} and ν_{O_2} modes at 2345 and 1555 cm⁻¹, respectively.

Because of the low numerical aperture of the long-working-distance 20× objective, a relatively long collection time of 1000 s was required. The highest power at the sample of the excitation laser that can be allowed, without substantially heating the sample, was 400–450 mW. To facilitate the comparison of the peak intensities of spectra recorded at various laser powers, all spectra are normalized with respect to the Raman band of N₂. This method also compensates for the effects of possible illumination nonuniformities at the sample.

III. Results and Discussion

III.A. MoO_x Nanowire Electrodeposition. As shown in Scheme 2, MoO_x nanowires are converted “in place” on the graphite surface to MoS₂ nanowires. The data presented below will show that the diameter and length of the MoO_x nanowires deposited in the first step of the E/C synthesis strongly influences the corresponding properties of the MoS₂ nanowires obtained in the second step. These MoO_x nanowires were prepared by ESED,^{58,59} the selective electrodeposition of MoO_x at step edges on the freshly cleaved graphite surface. ESED involved the reduction of MoO₄²⁻ from a basic, aqueous solution according to reaction 1. As shown in Figure 1a, basic aqueous solutions of MoO₄²⁻ show a quasi-reversible reduction with an onset at -0.70 V vs SCE. This voltammetric wave is associated with the deposition of MoO_x according to reaction 1 (see above).^{58,59} When this reduction was carried out potentiostatically at a potential of -0.75 to -0.85 V vs SCE, a steady-state deposition current of 30–40 $\mu\text{A cm}^{-2}$ was observed within 40–50 s in an unstirred solution with [MoO₄²⁻] = 1.0 mM (Figure 1b). If this steady-state current was associated purely with the deposition of hemicylindrical nanowires, the radius of these structures, $r(t)$, should increase according to^{58,59,61}

$$r(t) = \sqrt{\frac{2i_{\text{dep}}t_{\text{dep}}V_{\text{m}}}{\pi nFl}} \quad (3)$$

where i_{dep} is the deposition current density, t_{dep} is the deposition duration, V_{m} is the molar volume of the deposited material (19.8 cm³ mol⁻¹ for MoO₂), n is the number of electrons transferred for the deposition of each metal atom (2 according to eq 1), F is the Faraday constant (96485 C equiv⁻¹), and l is the total length of nanowires on the graphite surface. Figure 1c shows that a plot of the wire diameter versus $t^{1/2}$ is linear, as predicted by eq 3, for growth times ranging 16–400 s and wire diameters ranging 67–230 nm.⁶² Using the slope of this plot (10.46 nm s^{-1/2}), we can calculate the length of MoO_x nanowires per unit electrode area, l/A , by solving for l in eq 3. This calculation yields a value for l/A of 2.4 $\mu\text{m } \mu\text{m}^{-2}$, in good agreement with the wire length per unit area seen in the SEMs of Figure 1d–f.

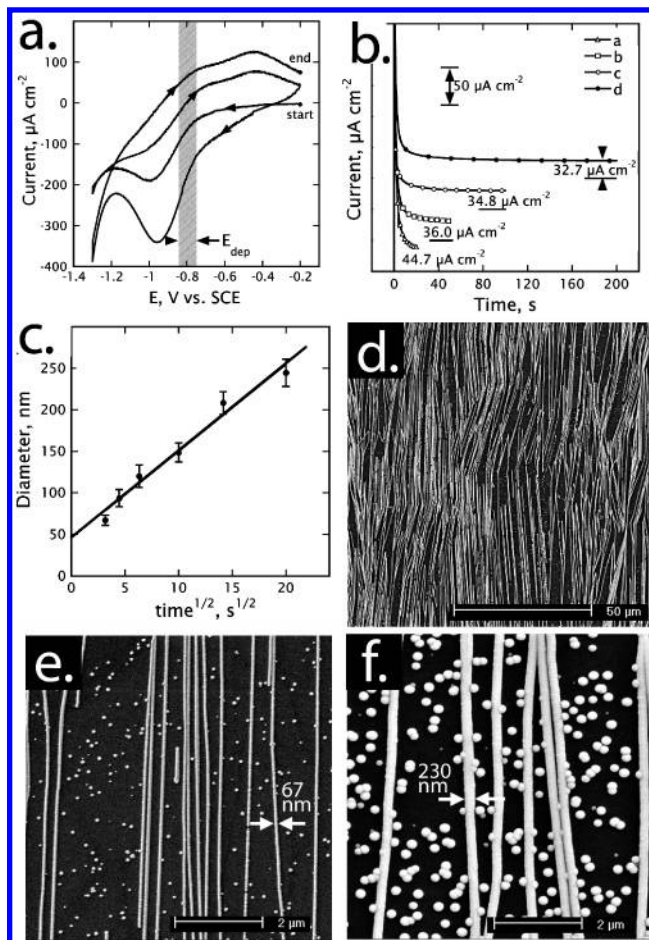


Figure 1. (a) Cyclic voltammograms at 20 mV s⁻¹ for an HOPG working electrode in an aqueous plating solution containing 1 mM Na₂MoO₄, 1.0 M NaCl, and 1.0 M NH₄Cl at pH 8.0. The hatched region shows the potential range employed for step-edge selective growth of MoO_x nanowires. (b) Current vs time for the electrodeposition of MoO_x nanowires at -0.80 V for durations of 25, 50, 100, and 200 s. These curves are distributed along the current axis for clarity; zero current for each is indicated as a horizontal bar. (c) Diameter of MoO_x nanowires as the measured by SEM plotted as a function of the square root of the deposition time. Error bars indicate $\pm 1\sigma$ in the diameter distribution. (d) Low-magnification SEM image of a graphite surface after the electrodeposition of MoO_x nanowires showing the parallel organization of these wires on the surface. (e and f) SEM images of MoO_x nanowires prepared using a deposition time of 25 s (e) and 200 s (f).

SEM images of MoO_x nanowires are shown in Figure 1d–f. Low-magnification images, like that of Figure 1d, show that MoO_x wires prepared by ESED were long with many longer than 50 μm , approximately straight, and organized into parallel arrays of hundreds of wires. Higher-magnification SEM images (Figure 1e,f) reveal these wires to be smooth and narrowly distributed in diameter. The distribution of wire diameters on a single surface was characterized by a relative standard deviation of 5–10%. MoO_x particles were also deposited in parallel with wires at an areal density of 10⁸–10⁹ cm⁻².

III.B. Conversion of MoO_x Nanowires to MoS₂ Nanowires. MoO_x nanowires were exposed to flowing H₂S at elevated temperatures between 500 and 1000 °C to effect the transformation to MoS₂ according to reaction 2. Within this temperature range, MoS₂ wires having either of two morphologies were obtained, as shown in Scheme 2: Temperatures in the range 500–700 °C produced low-temperature or LT MoS₂ nanowires that were nearly identical in size and shape to the MoO_x precursor wires. At temperatures from 800 to 1000 °C, MoS₂

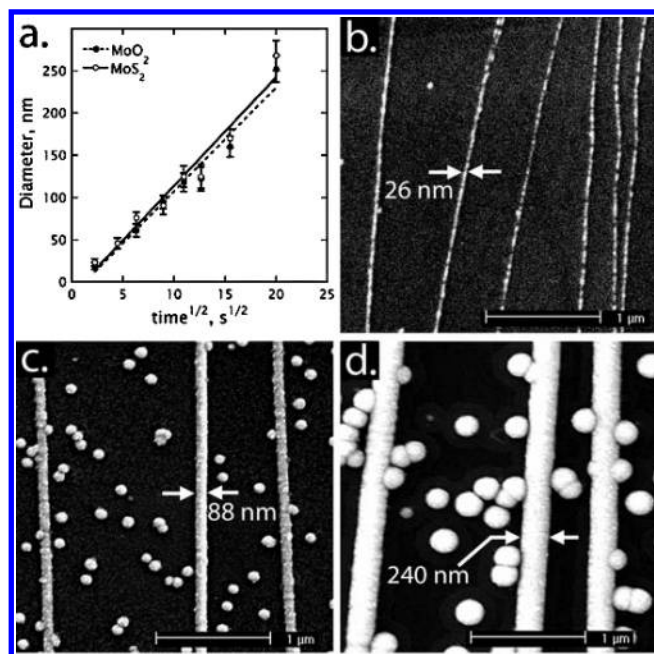


Figure 2. (a) Diameter of MoO_x and MoS₂ nanowires as measured by SEM plotted as a function of the square root of the deposition time. Error bars indicate $+1\sigma$ in the diameter distribution. (b–d) SEM images of MoS₂ nanowires obtained from MoO_x nanowires by conversion in H₂S at 700 °C for 24 h. The deposition times for the MoO_x precursor nanowires were as follows: 5 s (b), 80 s (c), and 400 s (d).

crystallites nucleated at the interface of the nanowire with the graphite surface. These crystallites were oriented with their *c*-axes perpendicular to the graphite surface and their basal planes in van der Waals contact with it. Growth of these crystallites away from the graphite/MoS₂ interface proceeded until the entire HT wire was converted to this highly oriented layered structure. This process coincided with a flattening of the (initially) hemispherical nanowire and the emergence of a ribbonlike morphology. We discuss the structure of the LT MoS₂ nanowires next, and then turn our attention to HT nanowires.

III.C. Structural and Chemical Characterization of LT MoS₂ Wires. At temperatures of 500–700 °C, MoO_x nanowires exposed to H₂S were converted quantitatively into MoS₂ nanowires. SEM images of typical LT MoS₂ nanowires are shown in Figure 2b–d together with a plot (Figure 2a) comparing the initial diameter of MoO_x precursor wires and the LT MoS₂ nanowires produced from these precursors. On the basis of the molar volumes of MoO₂ (19.7 cm³ mole^{−1}) and MoS₂ (32.4 cm³ mole^{−1}), and assuming that the expansion associated with conversion from MoO_x to MoS₂ is isotropic, the expected diameter ratio, $\text{dia}_{\text{MoS}_2}/\text{dia}_{\text{MoO}_x}$ will be $(32.4/19.8)^{1/3} = 1.18$. In agreement with this expectation, the mean diameter ratio derived from the data plotted in Figure 2a was 1.1 ± 0.1 . Except for this increase in diameter, LT MoS₂ nanowires appear in SEM images (Figure 2b–d) virtually identical to the MoO_x parent nanowires.

In addition to SEM, LT MoS₂ nanowires were characterized by XPS, TEM, selected area electron diffraction (SAED), X-ray powder diffraction (XRD), and Raman spectroscopy.

The Mo(3d) and S(2p) regions of the XPS spectrum for freshly deposited MoO_x nanowires and LT MoS₂ nanowires converted at 700 °C are shown in Figure 3. Freshly deposited MoO_x nanowires show binding energies for Mo(3d_{5/2}) electrons (Figure 3a; Table 1) in the range from 230.5 to 232.4 eV. These values are consistent with the findings of Swartz and Hercules⁶³ for MoO₂ (230.9 eV) and MoO₃ (232.5 eV) powders. We con-

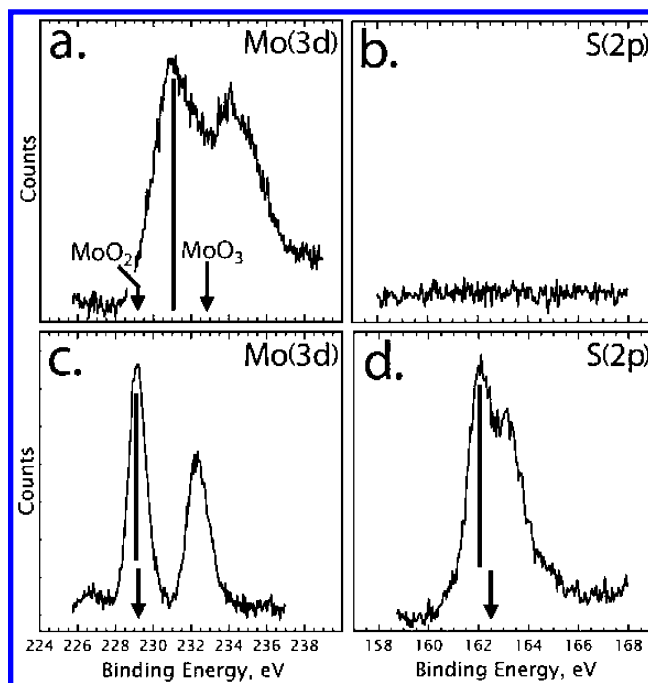


Figure 3. X-ray photoelectron spectra of graphite surfaces after the electrodeposition of MoO_x nanowires (a, b) and after the exposure of MoO_x nanowires to H₂S at 700 °C for 24 h (c, d). Arrows indicate the chemical shifts expected for the Mo(3d_{5/2}) peak expected for MoO_x and MoS₂ (a, c) and the expected S(2p_{3/2}) chemical shift expected for MoS₂ on the basis of the literature precedents discussed in the text, and tabulated in Table 1. Both samples were deposited for 200 s from a solution containing 1.0 mM MoO₄^{2−} (1 M NaCl, 1 M NH₄Cl, pH = 8.0) and consisted of nanowires approximately 150 nm in diameter. All binding energies were referenced to the C(1s) peak of the graphite at 284.5 eV.

TABLE 1: XPS Results for MoO_x and MoS₂ Nanowires and a Comparison to Reference Values

sample	binding energy (eV)	
	Mo (3d _{5/2})	S (2p _{3/2})
Electrodeposited Nanowires		
MoO _x	230.5–232.5	162.4
MoS ₂ ^a	229.1	162.1
Reference Values ^b		
elemental Mo	226.1	
MoO ₂	230.9	
MoO ₃	232.5	
MoS ₂	229.0–229.6	162.5
elemental S		164.0
sulfides		160.5–164.0
sulfites		165.5–167.5
sulfates		168.0–171.0

^a Nanowires converted at 700 °C. ^b Mo and MoO_x taken from ref 63, sulfur compounds from ref 60.

clude that the electrodeposited material is a mixture of Mo(IV) and Mo(VI) oxide.⁵⁹ Upon exposure of the MoO_x wires to H₂S at 700 °C, a sulfur peak appears with an S(2p_{3/2}) binding energy of 162.1 eV (Figure 3d), while the Mo(3d) peaks narrow and shift to lower energy with an Mo(3d_{5/2}) binding energy of 229.1 eV (Figure 3c). These values are similar to literature values reported for MoS₂ (see Table 1), and are consistent with a complete conversion of the electrodeposited MoO_x to MoS₂.

High-magnification SEM images of LT MoS₂ nanowires (Figure 4a) show a rougher surface than is seen for the parent MoO_x nanowires (Figure 1e,f). TEM images of these nanowires (Figure 4b) reveal that this roughness is a manifestation of the internal microstructure of the wire, which contains many

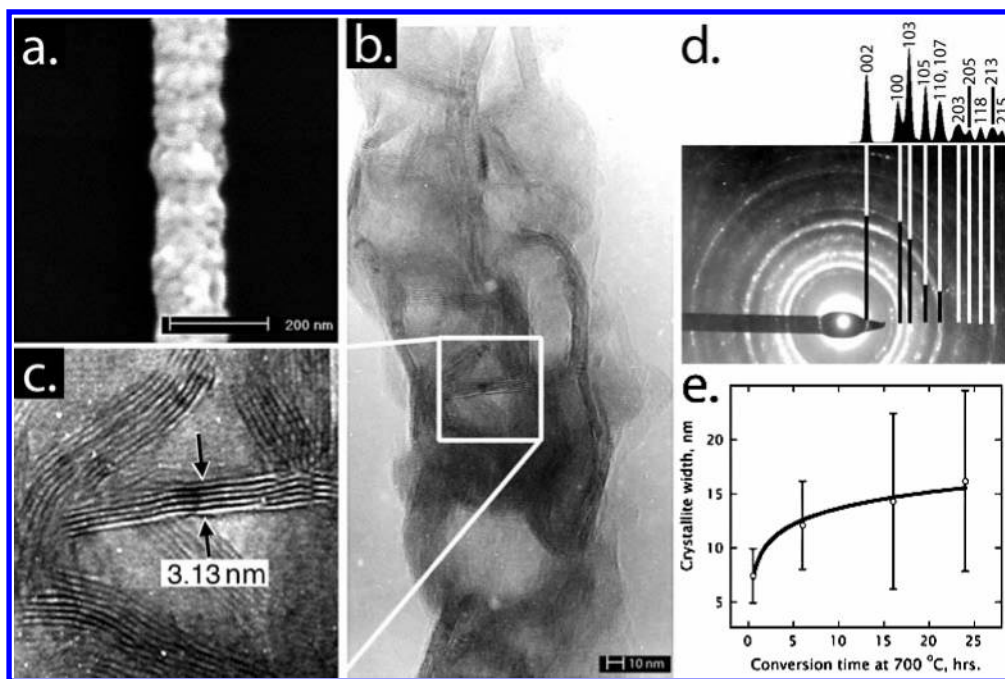


Figure 4. (a) SEM image of an MoS₂ nanowire prepared by conversion in H₂S at 500 °C for 24 h. (b) TEM image of an MoS₂ nanowire annealed in H₂S at 500 °C for 24 h. (c) Higher-magnification view of the indicated region of the TEM image of (b) showing ribbon morphology within nanowire. (d) SAED pattern of the MoS₂ nanowires annealed in H₂S at 500 °C for 24 h. At top is shown the electron intensity profile expected for 2H-MoS₂ nanocrystallites having a diameter of 10 nm. (e) Crystallite width measured by TEM as a function of annealing time at 700 °C in H₂S. Error bars indicate $\pm 1\sigma$ in the width distribution.

interwoven ribbons of MoS₂ that are 5–15 nm in width (e.g., 9–27 layers) and up to hundreds of nanometers in length. As shown in Figure 4c, stacks of van der Waals bonded MoS₂ layers, separated by 6.2 Å, are resolved in these TEM images, suggesting that these ribbons are crystalline. In contrast to electrodeposited MoO_x wires, which are amorphous by electron diffraction,⁵⁹ SAED of LT MoS₂ wires produced sharp powder diffraction patterns such as that shown in Figure 4d. The quality of this SAED pattern is sufficient to permit the polytype of these MoS₂ nanowires to be assigned as 2H (JCPDS 37-1492) on the basis of the presence of the (105) and (103) reflections for 2H and the absence of the (015) reflection characteristic of 3R-MoS₂ (JCPDS 17-0744).

As the duration of exposure to H₂S at 700 °C increases up to 24 h, TEM images reveal that the mean width of the MoS₂ crystallites increased from 8 to 16 nm (Figure 4e). The distribution of ribbon dimensions were broad for these samples, but ribbons with lateral dimensions greater than ~25 nm were not observed in TEM images even after exposures to H₂S at 700 °C of 24 h.

III.D. Structural Characterization of HT MoS₂ Wires. An increase from 700 to 800 °C in the temperature at which MoO_x nanowires were exposed to H₂S produced a very different morphology for the resulting MoS₂ nanowires. The evolution in morphology from the hemicylindrical MoO_x nanowires to the nanoribbon morphology obtained for MoS₂ at temperatures above 800 °C is shown in Figure 5. Here, the left-most column shows SEM images of MoO_x nanowires that were used as precursors. The two columns of images to the right of this show the MoS₂ nanowires produced from these MoO_x nanowires after 24 h of exposure to H₂S at 800 °C (middle images) and 84 h of exposure (right images). Basal layers of MoS₂, formed in van der Waals contact with the graphite surface, begin to emerge from the edges of the nanowires at 24 h. Atop these basal layers are “supernatant” crystallites of MoS₂. These are gradually consumed as the basal layers grow in both width and height. In

the images of Figure 5, supernatant crystallites remain on the 350 nm nanowires shown at upper right, and to a lesser extent on the 283 nm wires below these, but they are completely absent from the 124 nm nanowires at bottom right. The basal crystallites shown in these SEM images span the width of the nanowire and extend along the axis of the nanowire for lengths of up to several microns.

HT MoS₂ nanowires prepared at 800 °C for 24 h with a width of ~250 nm are shown in the SEM images of Figure 6a. TEM was used to probe the orientation of supernatant MoS₂ crystallites seen atop these nanowires, and typical TEM images are shown at progressively higher magnification in Figure 6b–d. These data showed that supernatant crystallites were virtually always oriented edge-on relative to the electron beam, perpendicular to the orientation of the basal layers. In contrast to LT MoS₂ nanowires, the supernatant crystallites seen by TEM atop HT MoS₂ nanowires were planar and up to hundreds of layers in thickness. The orientational difference between basal layers and supernatant crystallites may account for the pronounced image contrast seen in SEM images such as those shown in Figure 6a as well as in Figure 5.

For HT MoS₂ nanowires that were exposed to H₂S for longer durations of 84 h or more, supernatant crystallites were infrequently observed (e.g., Figure 7b), and TEM images of these nanowires (Figure 7a) showed polygonal regions that were of nearly uniform gray-scale indicative of crystallites of MoS₂. SAED (data not shown) showed only in-plane periodicities, which are very similar for 2H and 3R polytypes, because the electron beam was along the *c*-axis for these nanoribbons. The polytype of HT MoS₂ nanowires could not be established using either electron or X-ray diffraction because of the small quantity of material synthesized in these experiments, and because of the similarity of the diffraction patterns for 3R and 2H. However, visible–NIR absorption spectra, discussed later, provide evidence that HT MoS₂ nanowires are predominantly 3R. HT MoS₂ nanowires for which the conversion from supernatant crystallites

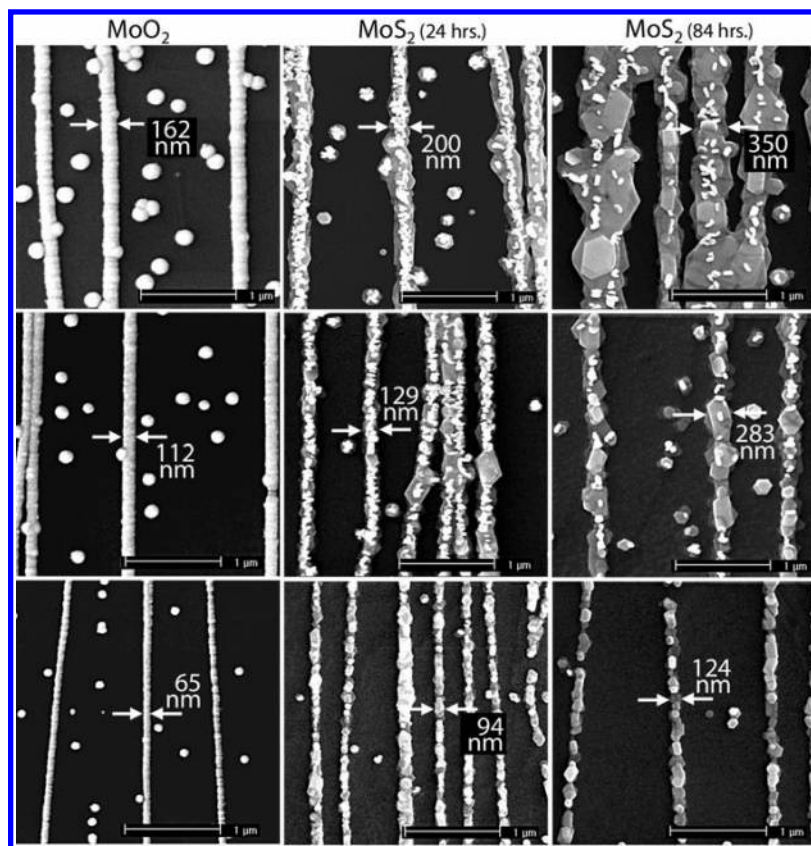


Figure 5. SEM images showing the evolution in morphology for MoO_x nanowires (left images) following exposure to H₂S at 800 °C in H₂S for 24 h (center images) and 84 h (right images). The MoO_x nanowires were prepared using t_{dep} of 50, 100, and 200 s.

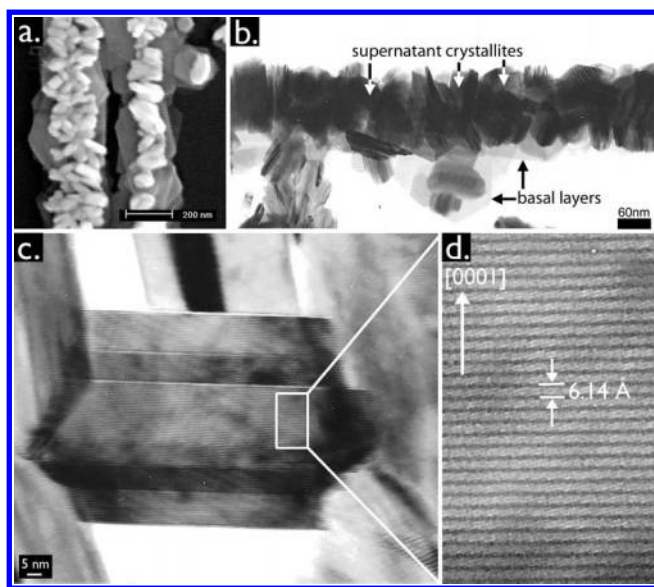


Figure 6. (a) SEM image of HT MoS₂ nanowires prepared at 800 °C for 24 h. (b) TEM image of an HT MoS₂ nanowire prepared at 800 °C for 24 h. The basal MoS₂ layer and supernatant MoS₂ crystallites are labeled. (c) TEM image of supernatant crystallite at high magnification and (d) blow-up of indicated area showing crystallographic orientation of this supernatant grain and the visible layer spacing along the *c*-axis.

to basal crystallites is complete are “nanoribbons” with an aspect ratio (height/width) of just 0.05–0.1. Figure 7c shows an atomic force microscopy (AFM) image of the 150 nm diameter MoS₂ nanowire. Cross-sections through this image (Figure 7d) reveal that the height of this nanowire varies from 32 nm to less than 10 nm along its length, with a mean height of 14 nm.

The SEM and TEM images of Figures 5–7 all show that the basal layers of HT MoS₂ nanowires have long straight edges.

These “facets” permit the orientations of nearby crystallites to be compared. The (0001) surfaces of graphite and MoS₂ both have hexagonal periodicity, so if basal MoS₂ layers assume a preferred epitaxial orientation on the graphite surface, the subtended angle between the straight edges of MoS₂ crystallites will be integer multiples of 30°. However, we find that the angles of adjacent MoS₂ crystallites are uncorrelated both for crystallites growing along nanowires and for MoS₂ islands that have nucleated on the basal plane away from step edges and which, therefore, have assumed an orientation that is not influenced by the presence of a graphite step edge. We conclude that MoS₂ does not assume a preferred orientation on the graphite surface. A possible reason for the absence of epitaxy is shown in Figure 8. Here, we plot the normalized energy, E/ϵ_0 , for an MoS₂ island in van der Waals contact with the graphite surface as a function of the angle as the island is rotated through 60°. While several minima are seen in this plot, these wells are comparable in depth, and all are much more shallow than the well depth calculated for an energy-minimized island of CdS on HOPG, a material that grows epitaxially on graphite.⁶⁴ From the atom locations shown for MoS₂ and CdS in Figure 8c,d, respectively, it is apparent that even at 28.4° (the angle of minimum energy), MoS₂ is essentially incommensurate with the hexagonal periodicity of the graphite surface, whereas CdS, at a 30° angle of rotation, achieves a high degree of coincidence with it.

It should also be noted here that the characteristic morphology of HT MoS₂ nanowires could not be obtained by annealing LT MoS₂ nanowires at 800–1000 °C in N₂. Instead, sublimation of MoS₂ occurred, leading to the “corroded” morphology, and the formation of fullerene nanoparticles were observed with closed MoS₂ layers. The presence of H₂S in the contacting gas phase at these temperatures suppressed sublimation at all temperatures below 1000 °C.

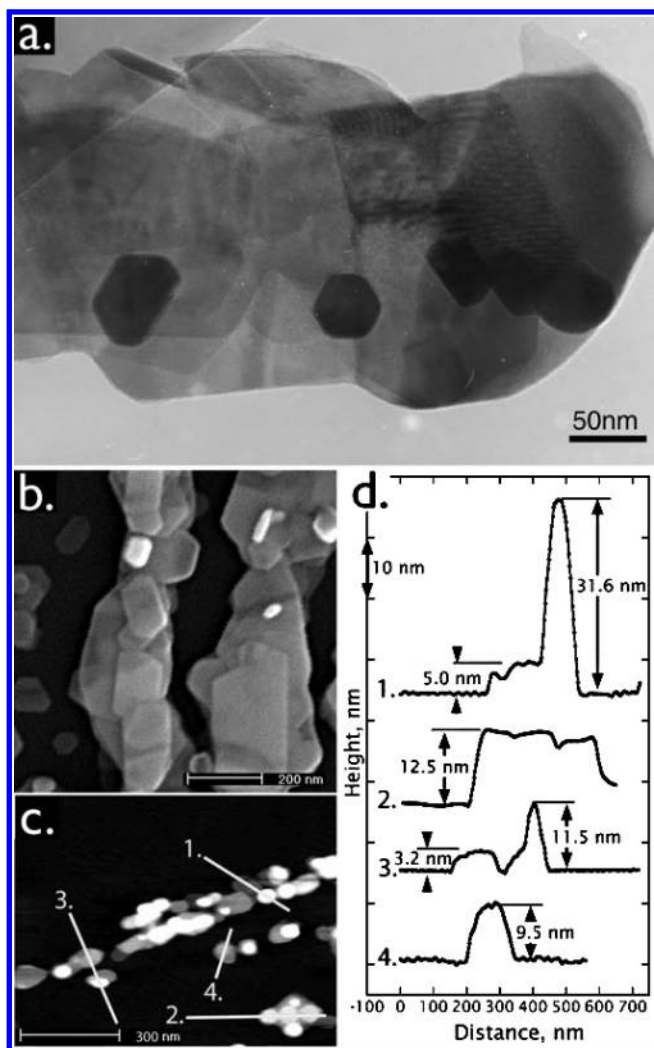


Figure 7. (a) TEM images of HT MoS₂ nanowire prepared at 800 °C for 84 h. (b) SEM image of an HT MoS₂ nanowire prepared at 800 °C for 84 h. Few supernatant crystallites remain atop these nanowires. (c) AFM image of an MoS₂ nanowire annealed at 800 °C in H₂S for 84 h. Z range: 40 nm. (d) AFM height profiles for the MoS₂ nanowire shown in (c).

Collectively, these data suggest that the conversion of MoO_x nanowires to HT MoS₂ nanowires occurs via two sequential steps. First, MoO_x is initially converted to MoS₂ wires composed of nanocrystals having dimensions of a few nanometers. MoS₂ wires are apparently trapped in this intermediate state at temperatures below 800 °C. At temperatures above 800 °C, a second step occurs involving the growth of MoS₂ grains. Grain growth is most rapid for basal layers of MoS₂ that are in van der Waals contact with the graphite surface; “supernatant” crystallites (those located atop this basal layer) also grew, but at a slower rate. The rapid growth of the basal MoS₂ layers eventually occurs at the expense of these supernatant crystallites, and their number decreases as a function of heating time. After all the supernatant crystallites were consumed, very thin MoS₂ ribbons (less than 10% of their width) composed of micron-scale crystallites (in the dimensions perpendicular to the *c*-axis) were obtained.

III.E. Spectroscopy of LT and HT MoS₂ Wires. Raman spectra for LT and HT nanowires are compared with bulk MoS₂ in Figure 9. Raman spectra for 2H- or 3R-MoS₂ are identical and show four first-order Raman transitions:^{65,66} E_{2g}² (32 cm⁻¹), E_{1g} (286 cm⁻¹), E_{12g} (383 cm⁻¹), and A_{1g} (408 cm⁻¹). E_{1g} is forbidden for backscattering experiments with observation

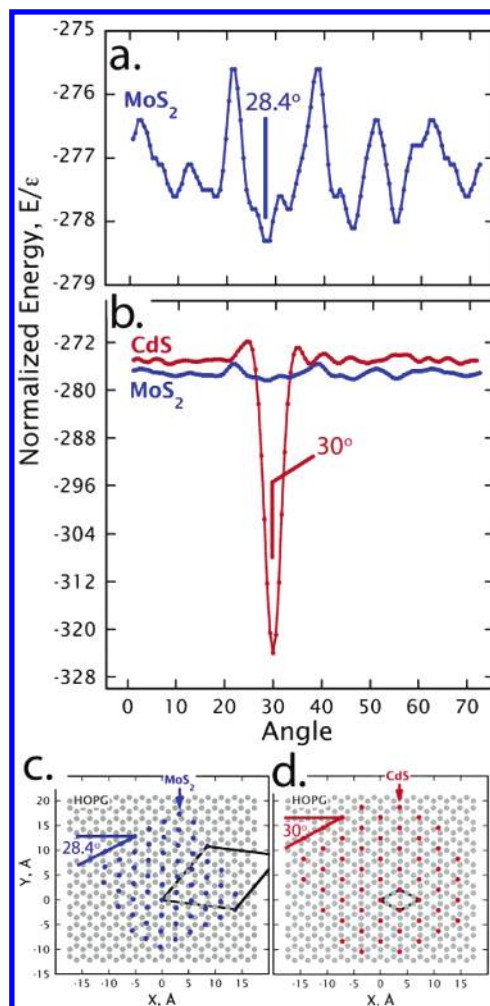


Figure 8. (a) Plot of the normalized energy (E/ϵ_0) vs angle for a two-layer-thick island of MoS₂ (blue circles) calculated using a Lennard-Jones 6-12 potential with well depth ϵ_0 . This MoS₂ island was approximately 20 Å in diameter and consisted of 124 atoms partitioned into two layers of equal size; the graphite surface also consisted of two layers, each containing 941 atoms. (b) Comparison of E/ϵ_0 vs angle for MoS₂ plotted in (a) with E/ϵ_0 vs angle calculated for the (0001) plane of wurtzite phase CdS (red), a material that grows on graphite with a strong epitaxial preference.⁶⁴ (c, d) Atom positions on the graphite surface corresponding to the angle that yielded the minimum energy for islands composed of MoS₂ (c) and CdS (d).

parallel to the *c*-axis, and this is the orientation here for both the bulk sample and the HT nanowires; however, E_{1g} was also absent in spectra of LT nanowires. E_{2g}² was too low in energy to be observed with our spectrometer. The spectra in Figure 9 were acquired using an excitation wavelength of 514.5 nm (2.41 eV) that is 0.5 eV above the direct band gap at 1.95 eV. Prior work⁶⁶ has shown that, for excitation energies within 0.2 eV of the direct gap, many multiphoton Raman transitions are observed, leading to a complex Raman scattering spectrum, but the first-order spectra shown in Figure 9 are very similar to those seen previously^{e.g.,65,66} for MoS₂ with excitation at 530.5 or 514.5 nm. The two most intense peaks at 388 and 413 cm⁻¹ are assigned to E_{12g}(Γ) and A_{1g}(Γ), respectively, and are unshifted in the two nanowire samples. This provides another indication that these wires are composed of crystalline MoS₂. As shown in the inset to Figure 9, the width of these Raman scattering lines increased in the following order: bulk, HT, LT. A similar increase in line width was reported previously for MoS₂ nanoparticles.^{67–69} Increased line width for nanoparticles versus bulk MoS₂ crystals can be the result of wave-vector

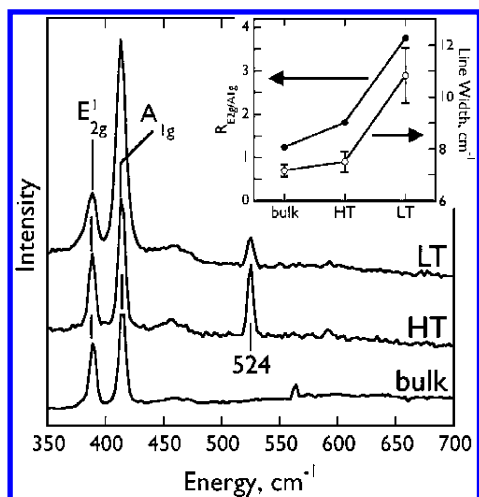


Figure 9. Raman spectra (nonresonant) acquired at room temperature with excitation at 514.5 nm for a bulk MoS₂ crystal (mixed 3R and 3H phases), and LT and HT nanowire samples as indicated. Inset: Plots of the ratio A_{1g}/E_{12g} (or “R”) and the line width for a bulk MoS₂ crystal, LT nanowires, and HT nanowires.

uncertainty caused by finite, nanometer-scale MoS₂ layers, or it can simply be a manifestation of particle size, shape, and structure inhomogeneity. A second observation is that the intensity ratio between the A_{1g} and E_{12g} peaks, $R_{A_{1g}/E_{12g}}$, increased in the order $R_{A_{1g}/E_{12g}}^{\text{bulk}} < R_{A_{1g}/E_{12g}}^{\text{HT}} < R_{A_{1g}/E_{12g}}^{\text{LT}}$ (Figure 9, inset). Our observed value for $R_{A_{1g}/E_{12g}}^{\text{bulk}}$ of 1.25 is in the range from 1.1 to 1.5 typically reported for MoS₂.^{65,67,70} E_{12g} and A_{1g} correlate with atom displacements that are orthogonal to one another, with A_{1g} involving out-of-layer, symmetric displacements of sulfur atoms along the c -axis and E_{12g} involving in-layer displacements of Mo and S atoms.⁷⁰ We suggest that $R_{A_{1g}/E_{12g}}$ may provide an indication of the degree of structural coherence along the c -axis direction, thereby serving as an “order parameter” for spectroscopically assessing the degree of order present in MoS₂ nanomaterials, but further work will be required in order to establish this correlation. The nanowire samples also show a peak at 524 cm⁻¹, which we tentatively assign to $E_{1g}(\text{M}) + \text{LA}(\text{M})$ in accordance with the assignment of Frey et al.⁶⁷ in the Raman spectra of “platelet-like” 3R-MoS₂ nanoparticles. We did not observe this peak for bulk MoS₂, nor has it been observed in the nonresonant Raman spectra of bulk MoS₂ previously.

The optical absorbance of the MoS₂ wires was probed both for LT and HT MoS₂ nanowires. Band structure calculations^{71,72} show that 2H- and 3R-MoS₂ both have indirect band gaps at ~1.20 eV, and a weak absorbance for MoS₂ beginning at 1.24 eV has been seen experimentally.^{e.g.,73} Optical studies of MoS₂^{73–77} have focused on two exciton transitions in the visible range at 1.8–2.1 eV. In 1967, Evans and Young⁷⁵ reported a quantum confinement effect (the first observation of this for any material) for macroscopic 2H-MoS₂ crystal quantum wells prepared by repeatedly cleaving macroscopic MoS₂ crystals using adhesive tape. Quantum confinement was manifested in the shift to higher energy of the A1 and B1 exciton peaks as the thickness was reduced gradually to 30 nm. In that work, the crystal thickness was determined by interferometry.

In this investigation, the optical absorbance of MoS₂ nanoribbons was probed either in transmission or reflection using an integrating sphere as described above. Absorption spectra for LT MoS₂ nanowires were acquired over the spectral range from 3.4 to 1.0 eV, but these spectra showed a broad absorption over this range with no well-defined direct absorption edge or

excitonic features. We do not discuss these data further here. Attention is focused instead on HT MoS₂ nanoribbons. Spectra for HT MoS₂ nanowires were acquired as a function of the thicknesses of these wires measured perpendicular to the graphite surface and parallel to the c -axis, L_{\perp} 's. L_{\parallel} was directly measured for each of 20 samples using AFM; the range of L_{\parallel} values was from 7 nm (11 layers) to 108 nm (176 layers). Spectra for thinner MoS₂ nanowires had insufficient signal-to-noise to permit the positions of the A1 and B1 excitons to be determined. A representative absorption spectrum for HT MoS₂ nanowires (Figure 10a) showed a well-defined absorption edge near the expected direct gap for MoS₂ of 1.95 eV (300 K⁷⁸), and A1 and B1 exciton transitions were observed at energies near this threshold in the 1.8–2.0 eV range as previously reported.^{e.g.,74,75,77–79} The presence of 2 exciton transitions near the direct band edges for 2H- and 3R-MoS₂ has been attributed^{e.g.,57} to spin–orbit splitting of the valance band.

The spectral range from 1.8 to 2.2 eV is shown in greater detail in Figure 10b for five samples of HT MoS₂ nanoribbons with L_{\parallel} ranging from 17 to 108 nm. A1 and B1 excitons are observed in each of these transmission absorption spectra, and the energy of these peaks increased with decreasing L_{\parallel} by 20–30 meV over this L_{\parallel} range. For thinner nanowires down to $L_{\parallel} = 7$ nm, reflection–absorption measurements were carried out, and energy shifts, ΔE_g 's, (versus the $L_{\parallel} = 108$ nm sample) as large as +80 meV for the B1 exciton were observed for nanoribbons with $L_{\parallel} = 7$ nm. Absorption spectra such as these provide direct evidence that the HT MoS₂ nanowires are predominantly 3R phase. As shown in Figure 10b, the energy of the B1 exciton, E_{B1} , is significantly different for 3R and 2H polytypes, with 2H higher by 41 meV. With increasing L_{\parallel} , the measured value of E_{B1} approaches this limit asymptotically, and the largest wires we measured showed E_{B1} identical to the expected value for 3R within the accuracy of our spectrometer (~2 meV at this energy). The A1 and B1 exciton lines are relatively broad, and we cannot exclude the possibility that some 2H is present in addition to 3R in these HT MoS₂ nanowires, but its presence is not detected in these absorption measurements.

In prior work, the spectral shift for quantum wells of layered metal dichalcogenides^{57,80} has been modeled using eq 4

$$\Delta E_g = \frac{\hbar^2 \pi^2}{2\mu_{\parallel} L_{\parallel}^2} \quad (4)$$

where ΔE_g is the shift in energy for an exciton (A1 or B1 in this study) measured relative to its energy in bulk MoS₂, μ_{\parallel} is the exciton effective mass in the direction parallel to the c -axis, and L_{\parallel} is the thickness of the quantum well measured along the c -axis.^{81–83} HT MoS₂ nanowires are expected to behave like quantum wells, not quantum wires, because these wires are a factor of 10 greater in width, (i.e., L_{\perp}) than in L_{\parallel} . This dimensional asymmetry is considerably larger than the asymmetry in the exciton Bohr radius, a_B , caused by the anisotropic structure of MoS₂. For example, Evans and Young⁷⁵ estimate that $a_B^{\perp} = 3.7$ and 1.3 nm for the A1 and B1 excitons, respectively, whereas these same values for the parallel direction are $a_B^{\parallel} = 2.4$ and 0.8 nm. We conclude that the confinement of charge carriers in the direction parallel to the c -axis will be much stronger than confinement perpendicular to it, and HT MoS₂ nanowires should behave as quantum wells.

Figure 10c shows that E_{A1} and E_{B1} increased in direct proportion to $1/L_{\parallel}^2$ in conformance with the predictions of eq 4. If eq 4 is used, the slopes of the straight lines shown in Figure

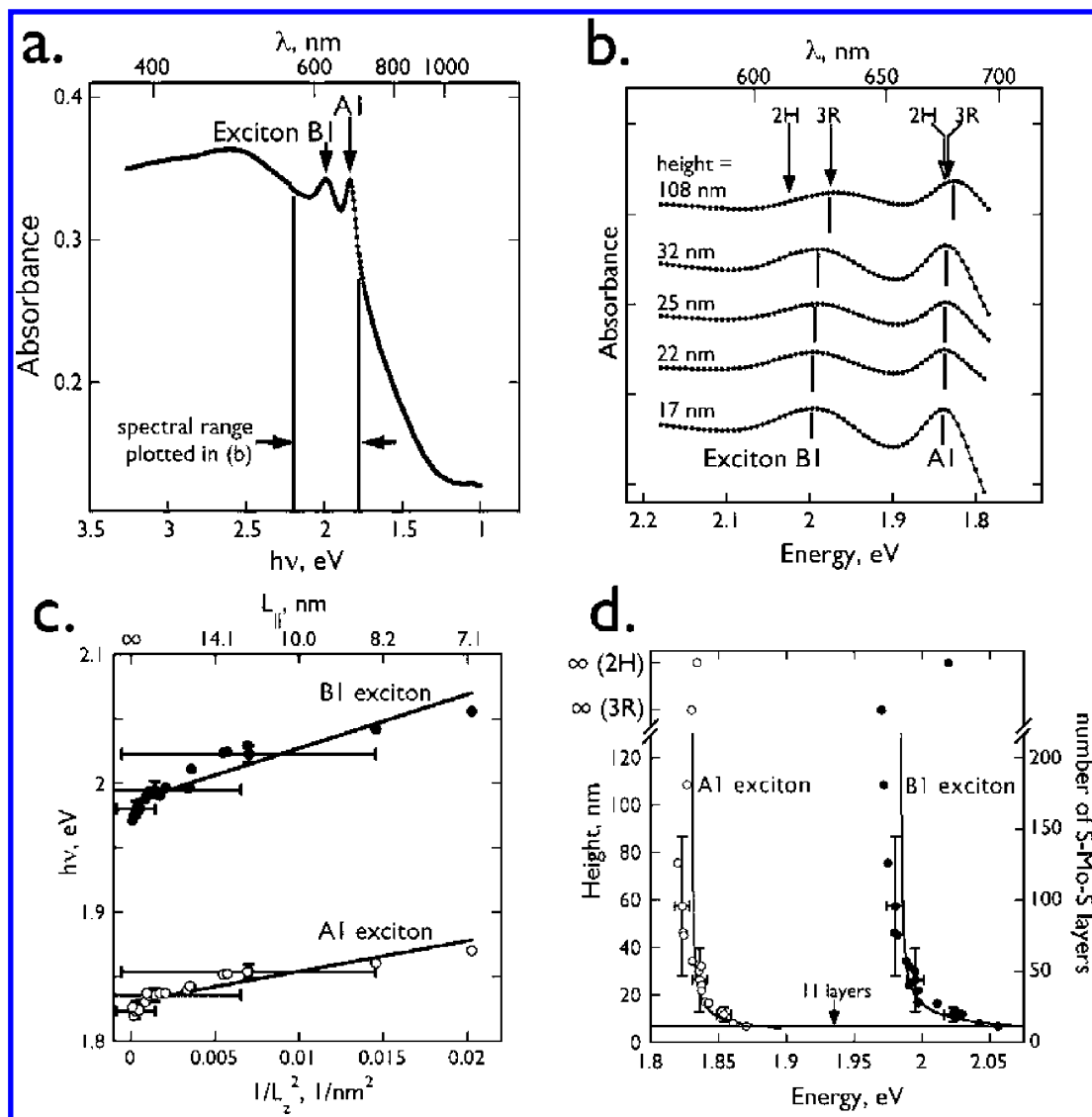


Figure 10. (a) Survey transmission-absorption spectrum for HT MoS₂ nanowires showing direct absorption edge and A1 and B1 exciton peaks. (b) Transmission-absorption spectra for the spectral interval shown in (a) for HT MoS₂ nanowires having five different thicknesses, $L_{||}$'s, from 17 to 108 nm. (c) Plot of ΔE vs $1/L_{||}^2$ for excitons A1 and B1. Solid lines are least-squares fits of eq 4 to these two data sets and yield $\mu_{||}^{A1} = 0.198m_0$ and $\mu_{||}^{B1} = 0.105m_0$. (d) Plot of $L_{||}$ as a function of peak energies for the A1 and B1 excitons. $L_{||}$ error bars are $\pm 1\sigma$ for AFM measurements on multiple wires in each sample; energy error bars correspond to ± 1.0 nm in wavelength. The solid lines are plots of eq 4 with $\mu_{||}^{A1} = 0.198m_0$ and $\mu_{||}^{B1} = 0.105m_0$.

TABLE 2: Effective Masses, $\mu_{||}$'s, of the Excitons A1 and B1 Parallel to the c -Axis: Comparison with Prior Results for 3R-MoS₂ and Fullerene MoS₂ Nanoparticles

ref	polytype/ T^a	$\mu_{ }^{A1}$	$\mu_{ }^{B1}$
Evans & Young ⁷⁵	3R/77 K (exptl)	$0.152m_0$	$0.440m_0$
Evans ⁹⁶	3R/77 K (exptl)	$1.28m_0$	$4.10m_0$
Coehoorn et al. ⁷²	3R/77 K (calcd)	$0.9m_0$	$3.2m_0$
Wilcoxon & Samara ⁴⁹	3R nanoparticles/300 K (exptl)	$0.16m_0^b$	n.a. ^b
Neville & Evans ⁸⁵	3R/77 K (exptl)	$0.037m_0$	$0.052m_0$
Frey et al. ⁶⁸	fullerene nanoparticles/25 K (exptl)	$0.92m_0$	$1.33m_0$
this work	3R/300 K (exptl)	$0.198m_0$	$0.105m_0$

^a The temperature at which spectra were acquired or calculated. ^b The nanoparticle shape, and its orientation relative to the illumination, were unknown. Therefore, the confinement direction was undefined.

10c yield effective mass values of $\mu_{||}^{A1} = 0.198m_0$ and $\mu_{||}^{B1} = 0.105m_0$, where m_0 is the electron mass. As shown in Table 2, our measured values of $\mu_{||}^{A1}$ and $\mu_{||}^{B1}$ are at the low end of values reported previously for 3R-MoS₂ and are an order of magnitude

smaller than $\mu_{||}$ values reported for fullerene MoS₂ nanoparticles. We are also among the first to measure a value for $\mu_{||}^{A1}$ that is greater than $\mu_{||}^{B1}$ (see comments below). As already indicated, excitons in MoS₂ are disc-shaped and have a larger exciton Bohr radius (and a smaller effective mass) perpendicular to the c -axis than parallel to it. The measured values of $\mu_{||}$ permit the Bohr exciton radius parallel to the c -axis of the MoS₂ lattice, $a_{b,||}$, to be calculated using⁸⁴

$$a_{b,||} = \frac{\epsilon_{||}}{(\mu_{||}/m_0)} a_0 \quad (5)$$

where m_0 is the electron mass, $\epsilon_{||}$ is the dielectric constant parallel to the c -axis ($\epsilon_{||} = 4.93^{85}$), and a_0 is the hydrogen Bohr radius (0.053 nm). For the A1 and B1 excitons, our measured values of $\mu_{||}$ yield $a_{b,||}$ values of 1.3 nm (A1) and 2.5 nm (B1). These values are similar in magnitude to those calculated by Evans and Young⁷⁵ (above), but the relative sizes of A1 and B1 are reversed. $L_{||}$ is plotted versus ΔE_g for both the A1 and

B1 excitons in Figure 10d for all 20 samples. In this plot, the solid lines are the predictions of eq 4 using the effective mass values derived from the analysis of Figure 10c and indicated in Table 2. It is apparent from this plot that the critical value of $L_{||}$ at which a blue-shift of the A1 or B1 excitons becomes measurable is $L_{||} \approx 25$ nm.

The absorption spectroscopy of fullerene MoS₂ nanowires has not been reported, but absorption spectra of fullerene MoS₂ nanoparticles prepared by Tenne and co-workers have been reported in two papers.^{68,69} Approximately spherical fullerene nanoparticles of MoS₂ also show A1 and B1 exciton peaks, but for nanoparticles with more than six layers ($n > 6$), these exciton transitions are red-shifted by up to 100 meV (for the B1 exciton) from bulk 2H-MoS₂. This surprising phenomenon is attributed⁶⁸ to the absence of a commensurate registry for adjacent MoS₂ layers within these nanoparticles. However, within a series of fullerene nanoparticles with wall thicknesses, L_w 's, ranging from 4 to 7 nm ($6 < n < 11$ layers), exciton peaks shifted smoothly to higher energy in direct proportion to $1/L_w^2$. Using a modified version of eq 4, the authors calculate mean reduced exciton mass values (Table 2) that are an order of magnitude larger than those we report for $\mu_{||}$.^{68,69} A detailed interpretation of this disparity is difficult because of uncertainties implicit in the application of eq 4 to the curved surfaces present in these fullerene nanoparticles.

The absorption spectroscopy of non-fullerene nanoparticles of MoS₂ has been reported in three previous papers: Nozik and co-workers⁴⁷ examined 1–3.5 nm diameter MoS₂ particles, Chikan and Kelley⁵⁰ studied 3.5, 4.5, and 8 nm diameter particles, and Wilcox et al.^{48,49} studied size-selected MoS₂ particles in the diameter range from 2 to 15 nm. The MoS₂ nanoparticles prepared and probed by the Nozik group were significantly smaller than the thinnest MoS₂ nanowires we probed in this study ($L_{||} = 7$ nm), and the structure of these particles could not be determined. Nozik et al.⁴⁷ reported an absorption onset between 3.2 and 3.5 eV, approximately consistent with the expected blue-shift in absorbance based on eq 4 and effective mass values tabulated in Table 2. Detailed correlations of these spectra with particle size were not attempted within this size regime.⁴⁷ Chikan and Kelley studied MoS₂ clusters consisting of a single MoS₂ layer (i.e., T-MoS₂),⁵⁰ and their spectra cannot, therefore, be directly compared with our absorption spectra for multilayer 3R-MoS₂ ribbons.

The spectroscopic data of Wilcox et al.^{48,49} is for (apparently) multilayer MoS₂ nanoparticles within a diameter range that overlaps the $L_{||}$ range we achieved for our nanowires, and here, a comparison can be more meaningful. In that paper, well-defined A1 and B1 exciton transitions are preserved, but blue-shifted, for particles with diameters down to 4.5 nm, and this result is consistent with our observations of A1 and B1 excitonic features for nanowires down to $L_{||} = 7$ nm (Figure 10). An approximately linear correlation of excitonic transitions with $1/D^2$ (where D is the particle diameter) was confirmed down to $D = 4.5$ nm. Although the confinement direction was undefined for the MoS₂ nanoparticles in those studies, an overall effective mass for the A1 exciton of $0.16m_0$ was derived from this slope using eq 4,⁴⁹ and this is close to our result. In one of their two papers,⁴⁸ Wilcox et al. present spectroscopic data (their Figure 8) which is consistent with a lower effective mass for the B1 exciton than for A1 (just as we report here in Table 2), but in that paper, the numerical values for μ^{B1} and μ^{A1} were not separately calculated.⁴⁸

III.F. Electrical Conduction in LT and HT MoS₂ Wires.

As shown in the SEM images of Figure 1d–f, the hundreds of

step edges present within a single HOPG grain show a tendency to be oriented parallel with one another. After MoS₂ nanowires are prepared on these surfaces, these nanowires were transferred to cyanoacrylate-coated glass surfaces without disrupting this alignment. The procedure for accomplishing this transfer⁸⁶ involves physically pressing the face of the HOPG crystal covered with nanowires onto a liquid cyanoacrylate droplet and permitting this droplet to harden over the course of 8 h. Upon lift-off of the graphite crystal, virtually all of the nanowires present on the graphite surface remain embedded at the surface of the cyanoacrylate disk. Low- and high-magnification SEM images of LT MoS₂ nanowires transferred in this way to a glass slide are shown in Figure 11a,b. Nanowires are inverted in the process of transfer so that the surface of the nanowires seen in these SEMs is the flat surface that was in contact with the graphite surface prior to transfer.

The electrical properties of ensembles of these nanowires were probed by evaporating gold current collectors onto the ends of wire arrays, as shown in Figure 11c. Current versus voltage curves were then acquired as a function of temperature over the range from 240 to 320 K. For all of the tested devices, the resistance of LT nanowire devices ranged from 200 to 900 M Ω , while the resistance of HT nanoribbon devices ranged from 1.0 to 10 M Ω , approximately 2 orders of magnitude lower. While the number of nanowires active in these devices could not be precisely known or controlled, this number should be approximately the same for LT and HT nanowires and in the range from 360 to 600 based on SEM images of these devices. The data suggest that the resistance of HT nanowires is lower than that of LT MoS₂ nanowires, and there can be 2 reasons for this disparity, both of which are related to the morphology of these nanowires. For HT MoS₂ nanowires, the orientation of basal grains allows for current flow in the direction perpendicular to the c -axis of the MoS₂ unit cell. This is the lowest resistance path possible: compared with the conductivity measured along the c -axis, the conductivity measured perpendicular to the c -axis is 200 times greater.⁸⁷ Within LT MoS₂ nanowires, MoS₂ crystallites are isotropically oriented with respect to the wire axis (see Figure 4b,c), and electrons can be expected to take a path of higher resistance through crystallites having a distribution of orientations. A second contributing factor is the grain size (much larger for HT MoS₂ nanowires) and the contributions of grain boundaries to the nanowire resistance. In fact, there is reason to believe that the overall resistance of these nanowires derives primarily from grain boundaries, and we discuss this in greater detail below.

The I – V curves plotted in Figure 11g show that the conductivity of MoS₂ nanowires increases with temperature, which is consistent with the semiconducting nature of MoS₂ and suggests a thermally activated conduction mechanism. These data permit the calculation of an activation energy for conduction, Φ_B , but not the electrical conductivity of individual nanowires, because the number of electrically continuous nanowires participating in conduction was not known, and because the contact resistance could not be eliminated in this two-terminal configuration. Nanowire ensembles of three types were examined: LT MoS₂ nanowires (shown in Figure 11d), HT MoS₂ nanowires for which significant supernatant MoS₂ crystallites were present (Figure 11e), and HT MoS₂ nanowires that were completely converted to basal-plane-oriented crystallites (Figure 11f). All three types of MoS₂ nanowires showed linear, ohmic I – V curves and a semiconductor-like temperature dependence characterized by a conductance ($\sigma = 1/R$) that

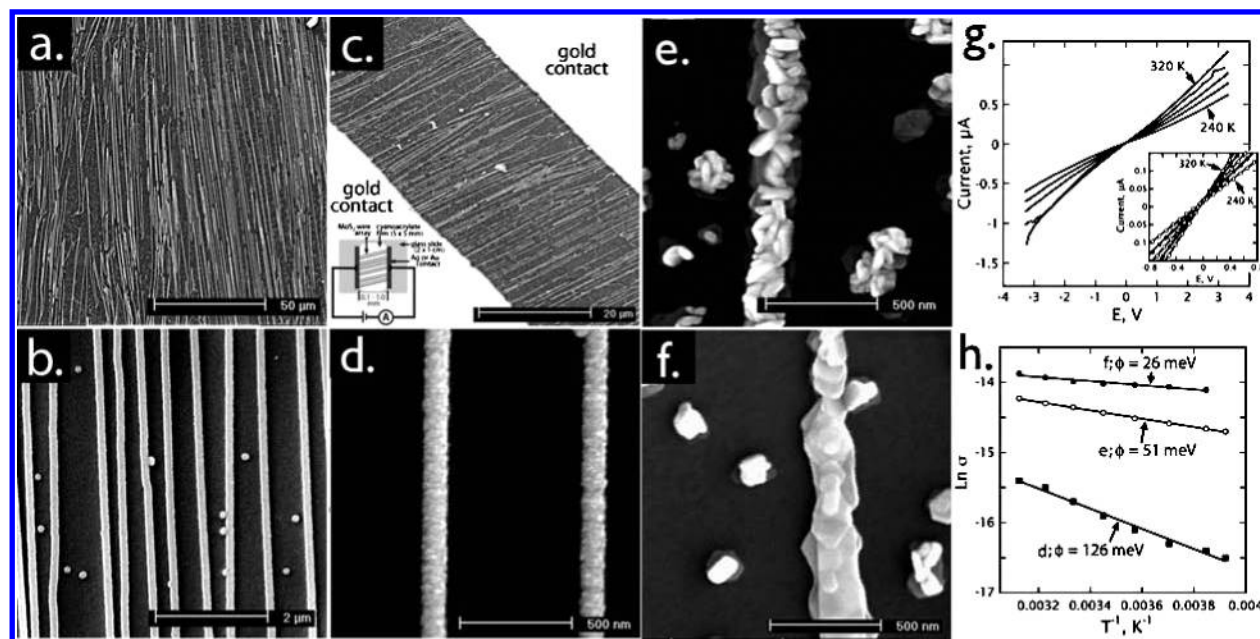


Figure 11. (a–b) SEM image of HT MoS₂ nanowire arrays on the adhesive surface at two magnifications. The surface was coated with 10 nm of gold for SEM imaging. (c) SEM image of an HT MoS₂ nanowire array after the evaporation of gold contacts. (d) LT MoS₂ nanowires prepared by MoO_x deposition for 150 s, followed by exposure to H₂S at 700 °C for 24 h. (e) HT MoS₂ nanoribbons prepared by MoO_x deposition for 100 seconds, followed by exposure to H₂S at 800 °C for 24 h. (f) HT MoS₂ nanoribbons prepared by MoO_x deposition for 100 seconds, followed by exposure to H₂S at 800 °C for 84 h. (g) Current vs voltage curves as a function of temperature for ensembles of HT MoS₂ nanowires prepared by heating in H₂S for 24 h. (h) $\ln \sigma$ plotted as a function of T^{-1} for the three MoS₂ nanowire ensembles shown in (d–f). σ is the conductance of the nanowire array measured by the current–voltage curve.

increased with temperature. Plots of $\ln(\sigma)$ versus $1/T$ (Figure 11h) are linear and in conformance with eq 6

$$\sigma = \sigma_0 \exp\left[\frac{-\Phi_B}{kT}\right] \quad (6)$$

where Φ_B is the thermal activation barrier for conduction, k is Boltzman's constant, and T is temperature. The slopes of these lines yield Φ_B values of 126, 51, and 26 meV for the MoS₂ nanowires shown in the SEM images of Figure 11d,e,f, respectively. While Φ_B has not been previously measured for MoS₂ nanowires, the Φ_B values we have measured are at the lower end of the range seen for bulk MoS₂ crystals.^{88–92} Because these barriers are much too small to correlate with the optical band gap for MoS₂ (near 1.9 eV), it has been proposed that they are extrinsic in origin and derived from the presence of impurity states near the band edges,⁹³ or from variations in the layer-to-layer spacing along the c -axis of the crystal.⁹¹ But these mechanisms cannot account for the correlation we have observed between Φ_B and the degree of order present in MoS₂ nanowires having the different morphologies, as documented in Figure 11.

A related issue is the magnitude of the electrical conductivity itself. A rough estimate of the resistance of a single HT MoS₂ nanowire like that shown in Figure 11f (250 nm in width, 25 nm in average height, and 29 μ m in length) can be obtained by multiplying the total resistance of the parallel ensemble of nanowires (1.19 M Ω) by the number of nanowires present in the device (\sim 2400) multiplied by the fraction of these that appear by SEM to be electrically continuous (15–25%). The result is 430–710 M Ω /nanowire, a value that is a factor of 30–50 higher than the resistance of 13.6 M Ω calculated using the physical dimensions of the nanowire and the known bulk resistivity of MoS₂ (3.4 Ω^{-1} cm⁻¹).⁹⁴ We conclude that electrical conduction in these HT MoS₂ nanowires is not controlled by the resistance of the MoS₂ crystallites, which should have the same conductivity as the bulk crystal, but by the grain boundaries present between these crystallites.

The electrical behavior of these MoS₂ nanowires resembles that of polycrystalline silicon, which also shows an anomalously large resistivity (relative to single crystalline material) and an activation energy for conduction that is much smaller than the band gap.⁹⁵ The grain boundary trapping theory (GBTT) devised by Sato⁹⁵ to account for these properties postulates that crystal defects present at grain boundaries, such as dangling bonds and misoriented planes, alter the band structure at the boundary region by creating trapping states below the conduction band.⁹⁵ Free carriers are trapped by these defect states, leading to a depleted region adjacent to each grain boundary. This depletion zone is responsible for a potential barrier that impedes the passage of charge carriers from one grain to the next. Application of GBTT to these polycrystalline MoS₂ nanowires leads to the expectation that the resistance of individual nanowires will be higher than the single crystal value, and that the activation energy associated with conduction will be directly proportional to the grain diameter, thereby explaining the decline in the measured Φ_B from 126 meV for LT wires to 26 meV for HT ribbons.

IV. Summary

We report the first synthesis of nanowires and nanoribbons having bulklike MoS₂ crystal structures. Our synthesis relies on the step-edge selective electrodeposition of MoO_x to form hemicylindrical nanowires on the basal plane of a highly oriented pyrolytic graphite crystal, followed by the conversion of these nanowires to MoS₂ in H₂S at elevated temperatures. The following are the main conclusions regarding the nature of the synthesis process and the properties of the resulting MoS₂ nanowires.

1. Two structural types of MoS₂ nanowires were obtained depending on whether the conversion in H₂S was carried out below 700 °C (hemicylindrical, nanocrystalline, 2H polytype) or above 800 °C (ribbonlike, microcrystalline, highly oriented, 3R polytype).

2. LT and HT MoS₂ nanowires are obtained with size selectivity, because the final dimensions of the nanowire depend on the dimensions of the MoO_x nanowire from which it was synthesized, and the diameter of the MoO_x nanowires is proportional to the square root of the electrodeposition duration. "Populations" of MoS₂ nanowires were narrowly dispersed in terms of their lateral dimensions. Typical relative standard deviation values for the wire heights, $L_{||}$'s, of HT MoS₂ nanoribbons, for example, were <20%.

3. This synthetic method produces ensembles of hundreds of MoS₂ nanowires that are approximately straight and organized into parallel arrays on the graphite surface. These nanowires adhere weakly to the graphite and may be transferred without loss of registry to cyanoacrylate-coated glass surfaces for electrical or optical characterization. Both types of nanowires can be extremely long (>100 μ m) and electrically continuous.

4. HT MoS₂ nanoribbons (but not LT nanowires) show optical absorption spectra in which the A1 and B1 exciton transitions characteristic of bulk MoS₂ are clearly observed. This is true even for HT MoS₂ nanoribbons consisting of just eleven layers ($L_{||} = 7$ nm). The energies of these exciton peaks increase from the value characteristic of bulk 3R-MoS₂ and in direct proportion to $1/L_{||}^2$. Our measurements yield effective mass values of $\mu_{||}^{A1} = 0.198m_0$ and $\mu_{||}^{B1} = 0.105m_0$, corresponding to exciton Bohr radii of 1.3 nm (A1) and 2.5 nm (B1).

5. Electrical contact has been made to these nanowires to enable electrical measurement. The temperature-dependent I – V data shows thermally activated conduction with activation energies that were dependent on the morphology of the nanowires and varied from 126 meV for LT nanowires to 26 meV for HT nanowires.

In this paper, we have exploited this capability to make electrical and optical measurements of these wires, but in the future, it is hoped that the "transportability" of 3R-MoS₂ nanowire arrays may facilitate the incorporation of these nanowires in devices such as photoconductive optical detectors and chemical sensors.

Acknowledgment. This work was funded by the NSF (grant DMR-0405477). J.C.H. acknowledges funding support from the Department of Energy (grant DE-FG03-96ER45576). J.A.S. acknowledges funding support by the NSF (grant CHE-0243424). The authors thank L. M. Yang and C. Cross for assistance with gold evaporation. Finally, we are grateful to Dr. Art Moore, formerly of GE Advanced Ceramics, Inc., for donations of graphite.

References and Notes

- (1) Kovtyukhova, N. I.; Martin, B. R.; Mbindyo, J. K. N.; Smith, P. A.; Razavi, B.; Mayer, T. S.; Mallouk, T. E. *J. Phys. Chem. B* **2001**, *105*, 8762.
- (2) Kim, J. R.; Oh, H.; So, H. M.; Kim, J.; Kim, J. J. *Physica E* **2003**, *18*, 225.
- (3) Peng, K. Q.; Huang, Z. P.; Zhu, J. *Adv. Mater.* **2004**, *16*, 73.
- (4) Björk, M. T.; Ohlsson, B. J.; Thelander, C.; Persson, A. I.; Deppert, K.; Wallenberg, L. R.; Samuelson, L. *Appl. Phys. Lett.* **2002**, *81*, 4458.
- (5) Kim, J. R.; Oh, H.; So, H. M.; Kim, J. J.; Kim, J.; Lee, C. J.; Lyu, S. C. *Nanotechnology* **2002**, *13*, 701.
- (6) Cui, Y.; Lieber, C. M. *Science* **2001**, *291*, 851.
- (7) Austin, M. D.; Chou, S. Y. *Nano Lett.* **2003**, *3*, 1687.
- (8) McAlpine, M. C.; Friedman, R. S.; Jin, S.; Lin, K. H.; Wang, W. U.; Lieber, C. M. *Nano Lett.* **2003**, *3*, 1531.
- (9) Harnack, O.; Pacholski, C.; Weller, H.; Yasuda, A.; Wessels, J. M. *Nano Lett.* **2003**, *3*, 1097.
- (10) Lao, J. Y.; Wen, J. G.; Ren, Z. F. *Nano Lett.* **2002**, *2*, 1287.
- (11) Gudiksen, M. S.; Lauhon, L. J.; Wang, J.; Smith, D. C.; Lieber, C. M. *Nature* **2002**, *415*, 617.
- (12) Zhong, Z. H.; Qian, F.; Wang, D. L.; Lieber, C. M. *Nano Lett.* **2003**, *3*, 343.
- (13) Kim, M.; Jeon, B. H.; Kim, J. Y.; Choi, J. H. *Synth. Met.* **2003**, *135*, 743.
- (14) Duan, X. F.; Huang, Y.; Cui, Y.; Wang, J. F.; Lieber, C. M. *Nature* **2001**, *409*, 66.
- (15) Wang, J. F.; Gudiksen, M. S.; Duan, X. F.; Cui, Y.; Lieber, C. M. *Science* **2001**, *293*, 1455.
- (16) Kind, H.; Yan, H. Q.; Messer, B.; Law, M.; Yang, P. D. *Adv. Mater.* **2002**, *14*, 158.
- (17) Huang, Y.; Duan, X. F.; Cui, Y.; Lieber, C. M. *Nano Lett.* **2002**, *2*, 101.
- (18) Cui, Y.; Zhong, Z. H.; Wang, D. L.; Wang, W. U.; Lieber, C. M. *Nano Lett.* **2003**, *3*, 149.
- (19) Huang, Y.; Duan, X. F.; Cui, Y.; Lauhon, L. J.; Kim, K. H.; Lieber, C. M. *Science* **2001**, *294*, 1313.
- (20) Kazes, M.; Lewis, D. Y.; Ebenstein, Y.; Mokari, T.; Banin, U. *Adv. Mater.* **2002**, *14*, 317.
- (21) Yan, H. Q.; He, R. R.; Johnson, J.; Law, M.; Saykally, R. J.; Yang, P. D. *J. Am. Chem. Soc.* **2003**, *125*, 4728.
- (22) Johnson, J. C.; Choi, H. J.; Knutsen, K. R.; Schaller, R. D.; Yang, P. D.; Saykally, R. J. *Nat. Mater.* **2002**, *1*, 106.
- (23) Johnson, J. C.; Yan, H. Q.; Yang, P. D.; Saykally, R. J. *J. Phys. Chem. B* **2003**, *107*, 8816.
- (24) Huang, M. H.; Mao, S.; Feick, H.; Yan, H. Q.; Wu, Y. Y.; Kind, H.; Weber, E.; Russo, R.; Yang, P. D. *Science* **2001**, *292*, 1897.
- (25) Johnson, J. C.; Yan, H. Q.; Schaller, R. D.; Haber, L. H.; Saykally, R. J.; Yang, P. D. *J. Phys. Chem. B* **2001**, *105*, 11387.
- (26) Duan, X. F.; Huang, Y.; Agarwal, R.; Lieber, C. M. *Nature* **2003**, *421*, 241.
- (27) Cui, Y.; Wei, Q. Q.; Park, H. K.; Lieber, C. M. *Science* **2001**, *293*, 1289.
- (28) Hahn, J.; Lieber, C. M. *Nano Lett.* **2004**, *4*, 51.
- (29) Lukes, F. *Surf. Sci.* **1972**, *30*, 91.
- (30) Rohkel, K.; Hartnagel, H. L. *Int. J. Electron.* **1986**, *60*, 663.
- (31) Mizokawa, Y.; Komoda, O.; Miyase, S. *Thin Solid Films* **1988**, *156*, 127.
- (32) Tanimoto, M.; Furuta, T.; Kuriyama, Y. *Jpn. J. Appl. Phys., Part 2* **1989**, *28*, L290.
- (33) Dallesasse, J. M.; Elzein, N.; Holonyak, N.; Hsieh, K. C.; Burnham, R. D.; Dupuis, R. D. *J. Appl. Phys.* **1990**, *68*, 2235.
- (34) Ross, S.; Sussman, A. *J. Phys. Chem.* **1955**, *59*, 889.
- (35) Tributsch, H. *Faraday Discuss.* **1980**, 189.
- (36) Tributsch, H. *Ber. Bunsen-Ges. Phys. Chem.* **1977**, *81*, 361.
- (37) Tributsch, H.; Gerischer, H.; Clemen, C.; Bucher, E. *Ber. Bunsen-Ges. Phys. Chem.* **1979**, *83*, 655.
- (38) Tributsch, H. *Sol. Energy Mater.* **1979**, *1*, 257.
- (39) Zak, A.; Feldman, Y.; Alperovich, V.; Rosentsveig, R.; Tenne, R. *J. Am. Chem. Soc.* **2000**, *122*, 11108.
- (40) Feldman, Y.; Frey, G. L.; Homyonfer, M.; Lyakhovitskaya, V.; Margulis, L.; Cohen, H.; Hodes, G.; Hutchison, J. L.; Tenne, R. *J. Am. Chem. Soc.* **1996**, *118*, 5362.
- (41) Remskar, M.; Skraba, Z.; Cleton, F.; Sanjines, R.; Levy, F. *Appl. Phys. Lett.* **1996**, *69*, 351.
- (42) Remskar, M.; Skraba, Z.; Cleton, F.; Sanjines, R.; Levy, F. *Surf. Rev. Lett.* **1998**, *5*, 423.
- (43) Remskar, M.; Skraba, Z.; Ballif, C.; Sanjines, R.; Levy, F. *Surf. Sci.* **1999**, *435*, 637.
- (44) Remskar, M.; Mrzel, A.; Skraba, Z.; Jesih, A.; Ceh, M.; Demsar, J.; Stadelmann, P.; Levy, F.; Mihailovic, D. *Science* **2001**, *292*, 479.
- (45) Zelenski, C. M.; Dorhout, P. K. *J. Am. Chem. Soc.* **1998**, *120*, 734.
- (46) Hsu, W. K.; Chang, B. H.; Zhu, Y. Q.; Han, W. Q.; Terrones, H.; Terrones, M.; Grobert, N.; Cheetham, A. K.; Kroto, H. W.; Walton, D. R. M. *J. Am. Chem. Soc.* **2000**, *122*, 10155.
- (47) Peterson, M. W.; Nenadovic, M. T.; Rajh, T.; Herak, R.; Micic, O. I.; Goral, J. P.; Nozik, A. J. *J. Phys. Chem.* **1988**, *92*, 1400.
- (48) Wilcoxon, J. P.; Newcomer, P. P.; Samara, G. A. *J. Appl. Phys.* **1997**, *81*, 7934.
- (49) Wilcoxon, J. P.; Samara, G. A. *Phys. Rev. B* **1995**, *51*, 7299.
- (50) Chikan, V.; Kelley, D. F. *J. Phys. Chem. B* **2002**, *106*, 3794.
- (51) Feldman, Y.; Wasserman, E.; Srolovitz, D. J.; Tenne, R. *Science* **1995**, *267*, 222.
- (52) Feldman, Y.; Margulis, L.; Homyonfer, M.; Tenne, R. *High Temp. Mater. Processes (London)* **1996**, *15*, 163.
- (53) Li, Q.; Newberg, J. T.; Walter, E. C.; Hemminger, J. C.; Penner, R. M. *Nano Lett.* **2004**, *4*, 277.
- (54) Penner, R. M. *Acc. Chem. Res.* **2000**, *33*, 78.
- (55) Gorer, S.; Hsiao, G. S.; Anderson, M. G.; Stiger, R. M.; Lee, J.; Penner, R. M. *Electrochim. Acta* **1998**, *43*, 2799.
- (56) Yang, D.; Sandoval, S. J.; Divigalpitaya, W. M. R.; Irwin, J. C.; Frindt, R. F. *Phys. Rev. B* **1991**, *43*, 12053.
- (57) Yoffe, A. D. *Adv. Phys.* **1993**, *42*, 173.
- (58) Zach, M. P.; Ng, K. H.; Penner, R. M. *Science* **2000**, *290*, 2120.
- (59) Zach, M. P.; Inazu, K.; Ng, K. H.; Hemminger, J. C.; Penner, R. M. *Chem. Mater.* **2002**, *14*, 3206.

- (60) Chastain, J. *Handbook of X-ray Photoelectron Spectroscopy*; Perkin-Elmer Corp.: Eden Prairie, MN, 1992.
- (61) Penner, R. M. *J. Phys. Chem. B* **2002**, *106*, 3339.
- (62) The plot of MoO₂ wire diameter vs time^{1/2} (Figure 1c) has a positive intercept on the diameter axis, because the deposition current at short times is larger than the steady-state i_{dep} value.
- (63) Swartz, W. E.; Hercules, D. M. *Anal. Chem.* **1971**, *43*, 1774.
- (64) Gorer, S.; Ganske, J. A.; Hemminger, J. C.; Penner, R. M. *J. Am. Chem. Soc.* **1998**, *120*, 9584.
- (65) Chen, J. M.; Wang, C. S. *Solid State Commun.* **1974**, *14*, 857.
- (66) Stacey, A. M.; Hodul, D. T. *J. Phys. Chem. Solids* **1985**, *46*, 405.
- (67) Frey, G. L.; Tenne, R.; Matthews, M. J.; Dresselhaus, M. S.; Dresselhaus, G. *Phys. Rev. B* **1999**, *60*, 2883.
- (68) Frey, G. L.; Elani, S.; Homyonfer, M.; Feldman, Y.; Tenne, R. *Phys. Rev. B* **1998**, *57*, 6666.
- (69) Frey, G. L.; Tenne, R.; Matthews, M. J.; Dresselhaus, M. S.; Dresselhaus, G. *J. Mater. Res.* **1998**, *13*, 2412.
- (70) Wieting, T. J.; Verble, J. L. *Phys. Rev. B* **1971**, *3*, 4286.
- (71) Kasowski, R. V. *Phys. Rev. Lett.* **1973**, *30*, 1175.
- (72) Coehoorn, R.; Haas, C.; deGroot, R. *Phys. Rev. B* **1987**, *35*, 6203.
- (73) Goldberg, A. M.; Beal, A. R.; Levy, F. A.; Davis, E. A. *Philos. Mag.* **1975**, *32*, 367.
- (74) Frindt, R. F. *Phys. Rev. B* **1965**, *140*, A536.
- (75) Evans, B. L.; Young, P. A. *Proc. R. Soc. London, Ser. A* **1967**, *298*, 74.
- (76) Goto, T.; Kato, Y.; Uchida, K.; Miura, N. *J. Phys.: Condens. Matter* **2000**, *12*, 6719.
- (77) Fortin, E.; Francisco, R. *Phys. Rev. B* **1975**, *11*, 905.
- (78) Beal, A. R. *J. Phys. C* **1979**, *12*, 881.
- (79) Beal, A. R.; Knights, J. C.; Liang, W. Y. *J. Phys. C: Solid State Phys.* **1972**, *5*, 3540.
- (80) Consadori, F.; Frindt, R. F. *Phys. Rev. B* **1970**, *2*, 4893.
- (81) D'Andrea, A.; Del Sole, R. *Solid State Commun.* **1990**, *74*, 1121.
- (82) D'Andrea, A.; Del Sole, R. *Phys. Rev. B* **1990**, *41*, 1413.
- (83) A more sophisticated treatment by D'Andrea and Del Sole (refs 82 and 83) permits calculations of higher accuracy within this weak confinement regime $L_{\parallel} > 5a_{\text{B}}$, but required, materials-specific parameters have not been reported for either 2H- or 3R-MoS₂.
- (84) Brus, L. *J. Phys. Chem.* **1986**, *90*, 2555.
- (85) Neville, R. A.; Evans, B. L. *Phys. Status Solidi B* **1976**, *73*, 597.
- (86) Walter, E. C.; Favier, F.; Penner, R. M. *Anal. Chem.* **2002**, *74*, 1546.
- (87) Wilson, J. A.; Yoffe, A. D. *Adv. Phys.* **1969**, *18*, 193.
- (88) Revolinsky, E.; Beerntsen, D. *J. Appl. Phys.* **1964**, *35*, 2086.
- (89) Mansfield, R.; Salam, S. A. *Proc. Phys. Soc. B* **1953**, *66*, 377.
- (90) Souder, A.; Brodie, D. E. *Can. J. Phys.* **1971**, *49*, 2565.
- (91) Harper, P. G. *J. Phys. C* **1974**, *1974*, 1247.
- (92) Evans, B. L.; Young, P. A. *Proc. R. Soc. London, Ser. A* **1965**, *A284*, 402.
- (93) El-Mahalawy, S. H.; Evans, B. L. *Phys. Status Solidi B* **1977**, *79*, 713.
- (94) Wieting, T. J. *J. Phys. Chem. Solids* **1970**, *31*, 2148.
- (95) Seto, J. Y. W. *J. Appl. Phys.* **1975**, *46*, 5247.
- (96) Evans, B. L. Optical and Electrical Properties. In *Physics and Chemistry of Materials with Layered Structures*; Lee, P. A., Ed.; Riedel: Dordrecht, The Netherlands, 1976; p 1.